2D MATERIALS

Observation of Rydberg moiré excitons

Qianying Hu[1,2,3]†, Zhen Zhan[4,5]†, Huiying Cui[1,2], Yalei Zhang[4], Feng Jin[1], Xuan Zhao[1,2], Mingjie Zhang[1,2], Zhichuan Wang[1,2], Qingming Zhang[1,6], Kenji Watanabe[7], Takashi Taniguchi[8], Xuewei Cao[3], Wu-Ming Liu[1,2], Fengcheng Wu[4,9], Shengjun Yuan[4,9]*, Yang Xu[1,2]*

Rydberg excitons, the solid-state counterparts of Rydberg atoms, have sparked considerable interest with regard to the harnessing of their quantum application potentials, but realizing their spatial confinement and manipulation poses a major challenge. Lately, the rise of two-dimensional moiré superlattices with highly tunable periodic potentials provides a possible pathway. Here, we experimentally demonstrate this capability through the spectroscopic evidence of Rydberg moiré excitons (X_{RM}), which are moiré-trapped Rydberg excitons in monolayer semiconductor tungsten diselenide adjacent to twisted bilayer graphene. In the strong coupling regime, the X_{RM} manifest as multiple energy splittings, pronounced red shift, and narrowed linewidth in the reflectance spectra, highlighting their charge-transfer character wherein electron–hole separation is enforced by strongly asymmetric interlayer Coulomb interactions. Our findings establish the excitonic Rydberg states as candidates for exploitation in quantum technologies.

The Rydberg states of matter are ubiquitously encountered in various physical platforms, ranging from atoms to molecules to solids (*1*–*3*). They share common features as exemplified by Bohr's description of the highly excited hydrogen atoms. The large spatial extent of the Rydberg-state wave function promotes large dipole moments with substantially enhanced sensitivity to weak external fields. Over the past two decades, Rydberg atoms have drawn much more attention owing to the experimental developments in trapping and manipulation of cold atoms, facilitating the study of quantum many-body physics and quantum information processing (*4*–*8*). Similarly, as the high-order Coulomb bound states of electron–hole pairs emerged in semiconductors, Rydberg excitons have also been proposed to host various potential applications such as simulating the topological Haldane phase and implementing quantum optimization algorithms (*3*, *9*, *10*). Their solid-state nature allows for compatibility with modern semiconductor technologies. However, the requisite controllability on spatial trapping for Rydberg excitons can be difficult to achieve in bulk materials. In this work, we instead used two-dimensional (2D) semiconductor monolayers (specifically WSe_2), which have strong light–matter interaction and support excitonic Rydberg states to high orders (*11*–*16*).

In recent years, the Rydberg sensing technique has been applied to the detection of nearby exotic electronic states and phase transitions by the environmentally sensitive Rydberg excitons in atomically thin semiconductors (*17*–*19*). In this experiment, we placed 2D moiré superlattices [specifically twisted bilayer graphene (TBG); lower layer in Fig. 1] beneath the monolayer WSe_2 (upper layer in Fig. 1) to provide spatially periodic modulations. When the wavelength λ of the potential landscape created by TBG is smaller than (or just comparable to) the exciton size r_B [~7 nm for the 2s states (*14*)], the Wannier-type exciton's wave packet is spread over a few moiré unit cells and does not lose its mobile character, as illustrated on the left side of Fig. 1. The optical response of the system is dominated by the Rydberg sensing scheme (*17*, *20*).

To realize efficient trapping, the moiré potential must have a spatial profile ($\lambda \propto \frac{1}{\theta}$ at small twist angles θ) that is properly larger than the exciton size (illustrated on the right side of Fig. 1), as has been shown for the ground-state excitons in transition metal dichalcogenide (TMD) heterobilayers (*21*–*28*). In our system, the accumulated charges in the TBG AA sites could strongly attract the oppositely charged electron or hole of the loosely bound 2s exciton in WSe_2, thus achieving spatial confinements of Rydberg moiré excitons (X_{RM}) with in situ controllable interaction strength up to 75 meV tuned by the charge density. The potential wells generated by the periodic charge distribution of TBG in the strong coupling regime $\left(\frac{\lambda}{r_B} > \sim 2.4\right)$ render an analog of the optical lattices created by a standing-wave laser beam or arrays of optical tweezers for Rydberg atom trapping (*1*, *2*, *29*). Given the nanoscale size ($\ll r_B$) of the confining potential well, we would further elaborate that the rigid quantum impurity approximation (*29*–*36*) is no longer valid for Rydberg excitons. The X_{RM} realize electron–hole separation and exhibit the character of long-lived charge-transfer excitons.

Rydberg sensing

Figure 2A illustrates the typical device schematic. The directly contacted TBG and monolayer WSe_2 are encapsulated by hexagonal boron nitride (hBN) dielectrics and graphite electrodes where the gate voltages are applied. Because of the band misalignment between TBG and WSe_2, charge carriers are only doped into TBG, whereas WSe_2 remains charge neutral within the experimentally accessible gating range. We used a broadband light source to excite the electron–hole pairs in monolayer WSe_2 and detect their resonance energies through reflectance contrast ($\Delta R/R_0$) spectroscopy. A HeNe laser at 632.8 nm was used for the photoluminescence measurements. The energies of excitons carry information about dielectric screenings and interactions with the charges in TBG. More details on device fabrication and optical measurements can be found in (*37*).

We first examined the device with relatively large twist angles, meaning small λ/r_B. The doping-dependent reflectance contrast ($\Delta R/R_0$) spectrum of device D1 with $\theta = 10°$ TBG ($\lambda/r_B \approx 0.2$ for the 2s excitons) is shown in Fig. 2B. In contrast to the barely changed 1s exciton (the excitonic ground state of WSe_2 near 1.71 eV), the 2s exciton (resonance near 1.78 to 1.8 eV) red shifts and merges into the renormalized band edge with increasing carrier densities (n). This observation is similar to that seen in the monolayer graphene/WSe_2 system (*20*, *37*). For TBG with a twist angle as large as 10°, the low-energy band structure maintains the linear dispersion of isolated graphene. In such small λ/r_B limits, the neighboring 2D electron gas (10° TBG here) provides a uniform dielectric background to screen the Coulomb interactions in WSe_2. The Rydberg exciton (2s state here) energy can be safely expressed as the subtraction of the binding energy from the quasiparticle bandgap, both of which get renormalized by increasing the density of states in TBG. The exciton Rydberg states therefore become delicate dielectric sensors to probe the dielectric function and electronic compressibility of the neighboring TBG. See (*20*, *38*) for more details.

The Rydberg sensing scheme also works for the near-magic-angle TBG (device D2, $\theta = 1.14°$, $\lambda/r_B \approx 1.9$) as shown in Fig. 2D. The doping-dependent 2s state (near 1.75 to 1.78 eV) exhibits a symmetric sawtooth pattern around

[1]Beijing National Laboratory for Condensed Matter Physics, Institute of Physics, Chinese Academy of Sciences, Beijing 100190, China. [2]School of Physical Sciences, University of Chinese Academy of Sciences, Beijing 100049, China. [3]School of Physics, Nankai University, Tianjin 300071, China. [4]School of Physics and Technology, Wuhan University, Wuhan 430072, China. [5]Imdea Nanoscience, 28015 Madrid, Spain. [6]School of Physical Science and Technology, Lanzhou University, Lanzhou 730000, China. [7]Research Center for Functional Materials, National Institute for Materials Science, Tsukuba 305-0044, Japan. [8]International Center for Materials Nanoarchitectonics, National Institute for Materials Science, Tsukuba 305-0044, Japan. [9]Wuhan Institute of Quantum Technology, Wuhan 430206, China.
*Corresponding author. Email: s.yuan@whu.edu.cn (S.Y.); yang.xu@iphy.ac.cn (Y.X.)
†These authors contributed equally to this work.

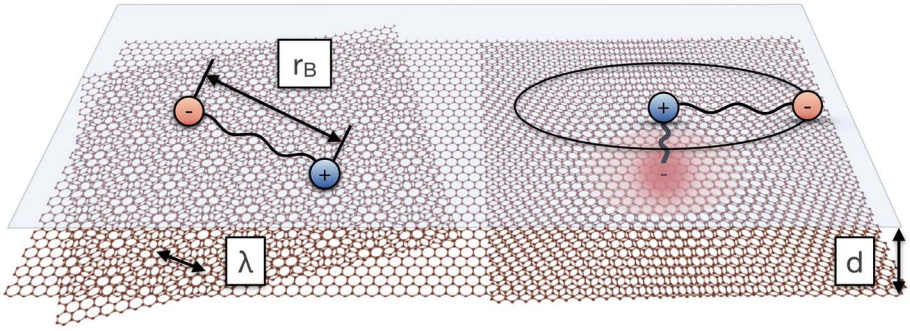

Fig. 1. Schematic illustration of the interplay between a Rydberg exciton (size r_B) and TBG moiré superlattices with small and large periodicity (wavelength λ). In the small λ/r_B limit (left panel), the moiré system provides a nearly uniform dielectric environment, and the optical response of the exciton is dominated by the Rydberg sensing features. The exciton maintains its mobile character. In the large λ/r_B limit (right panel), the Rydberg exciton can be confined by the moiré potential well generated by the accumulated charges in the AA site of TBG. The r_B is typically an order of magnitude larger than the interlayer spacing d, rendering much stronger interlayer interaction than the intralayer one in the formed Rydberg moiré exciton (X_{RM}) complex.

the zero density, with periodic intensity enhancements on both the electron and hole-doped sides, labeled as $\nu = -4, -3, \ldots, 3, 4$, respectively. Among them, the $\nu = \pm 4$ states correspond to the gap openings when the first moiré subbands of small-angle TBG are empty or fully filled, as schematically illustrated in the right panel of Fig. 2E. The features at full filling densities (denoted as n_s) allow us to determine the accurate twist angles in a wide range from ~0.73° to 1.6° in our devices (*37*).

On the other hand, the $\nu = \pm 3$ (± 2, ± 1, and 0) states, corresponding to 3 (2, 1, and 0) charges per moiré site, are beyond the scope of single-particle band theory. In the right panel of Fig. 2D, these features show little temperature dependence in the range of 1.6 to 10 K, well above the onset of correlated insulating states observed by transport measurements (*39*, *40*). They are consistent with the observations by scanning tunneling microscopy and local electronic compressibility measurements (*41*, *42*), both of which reveal a cascade of fourfold (spin and valley degrees of freedom) symmetry-broken states. We have observed these states with a twist angle ranging from 1.06° to 1.15°, demonstrating the prominent role of electronic correlations in the near-magic-angle TBG with band flattening (*39*–*45*).

In addition to the Rydberg sensing features discussed above, the spatially periodic dielectric screening environment provided by TBG modulates the spectrum as well. The emergence of the replica at higher energies (differ by Δ) is a manifestation of the formation of moiré bands in WSe_2 (*20*). additional optical transitions between states at high-symmetry points of the mini-Brillouin zone boundary become allowed above the fundamental bandgap, as shown by the schematic in the left panel of Fig. 2E (*20*). The mechanism is similar to the emergence of additional bright resonances due to the Bragg-Umklapp scatterings in the exciton dispersion picture (*46*, *47*). The experimentally observed energy separation between the 2s state (or band edge) and its replica Δ is ~32 meV, slightly larger than the value $\hbar^2/6m_r\lambda^2$ = 22 meV (where $\hbar$ is Planck's constant, and the reduced exciton mass m_r is ~0.15 free electron mass) expected from the weak perturbation limit.

Rydberg moiré excitons at smaller twist angles

When the twist angle θ is further reduced, we observe a pronounced enhancement of the interlayer Rydberg exciton-charge interactions, indicating access to the strong coupling regime. Similar reflectance spectrum measurements in device D3 with θ ≈ 0.6° TBG (λ ≈ 23.5 nm, $\lambda/r_B \approx 3.6$) is shown in Fig. 3A. Upon doping the TBG with either positively or negatively charged carriers, the 1s resonance only slightly shifts, whereas the 2s state near 1.783 eV splits into multiple branches and shows nonmonotonic doping dependencies. We focus on the 2s state in the following paragraphs, and the detailed discussion on other excitonic states is presented in (*37*). The resonance energies red shift first and then blue shift, reaching their minima at densities $n_m \approx 3.8 \times 10^{12}$ cm^{-2} for the electron-doped side and -4.7×10^{12} cm^{-2} for the hole-doped side. Some of the main branches could survive at relatively high temperatures up to 140 K, as shown in fig. S5. The splitting behavior reminds us of the multiple peaks of the ground-state moiré excitons observed in the TMD heterobilayers, suggesting that the exciton wave function resides at different moiré stacking sites and experiences inequivalent potentials (*20*–*27*). We attribute our observations to the formation of Rydberg moiré excitons (X_{RM}).

The photoluminescence measurements are presented in Fig. 3B, where only the lowest-energy branch of the X_{RM} shows bright emission and follows an almost identical trend to that in Fig. 3A. Such a prominent doping dependence is, at first sight, notable. The lowest-energy X_{RM} approaches the 1s exciton resonance, by only ~10 meV larger at n_m. The energy shift magnitude $|E_{shift}|$ from the charge neutrality point is extracted in Fig. 3C, where the carrier density is normalized by its full filling density $n_s = 8.37 \times 10^{11}$ cm^{-2}. It shows a nearly linear dependence on the density for $|n/n_s| < \sim 4$, as guided by the dashed lines in Fig. 3C. The $|E_{shift}|$ reaches its maximum energy shift E_m = 73 meV on the electron-doped side, which is much larger than the internal electron–hole binding energy of the 2s state (~9 meV for the WSe_2 in proximity to undoped TBG) (*37*). A simple dielectric screening cannot account for such large energy shifts.

The interaction between an exciton and a uniform Fermi sea has been extensively studied (*29*–*36*). The conventional wisdom of dealing with the exciton is treating it as a rigid and mobile impurity in a degenerate Fermi system. However, such an assumption is no longer valid here owing to the large spatial extension of the Rydberg excitons and the presence of long-wavelength moiré potentials. Because the change in intralayer binding energy is much smaller compared with the interlayer interaction, the energy shift of X_{RM} reflects the Coulomb interaction energy between the 2s exciton and free charges in TBG. A plausible explanation is related to the spatially confined charge distributions in TBG that can help promote unequal interlayer interactions for the constituent electron and hole of the exciton.

We hence carried out numerical simulations to extract the real-space charge distribution in TBG at different doping levels, as shown in Fig. 3E [see (*37*) and figs. S6 to S8 for further information]. Starting from the charge neutral point, the local charge density rises drastically at the AA-stacked regions first, while it is merely changed at the AB/BA-stacked regions. This is closely related to the much larger local density of states (LDOS) of the AA site at small densities. While the AA-stacked region has a radius of ~2.6 nm (estimated from the full width at half maximum of the spatially enhanced charge accumulation peak) that is much smaller than r_B, the areas of the AB/BA stacked region are greatly enlarged owing to lattice reconstruction (with the schematic superlattices shown in the lowest map in Fig. 3E) (*48*). Taking the electron-doped side as an example, the accumulated charges centered at the AA-stacked region create deep and narrow potential wells for trapping the

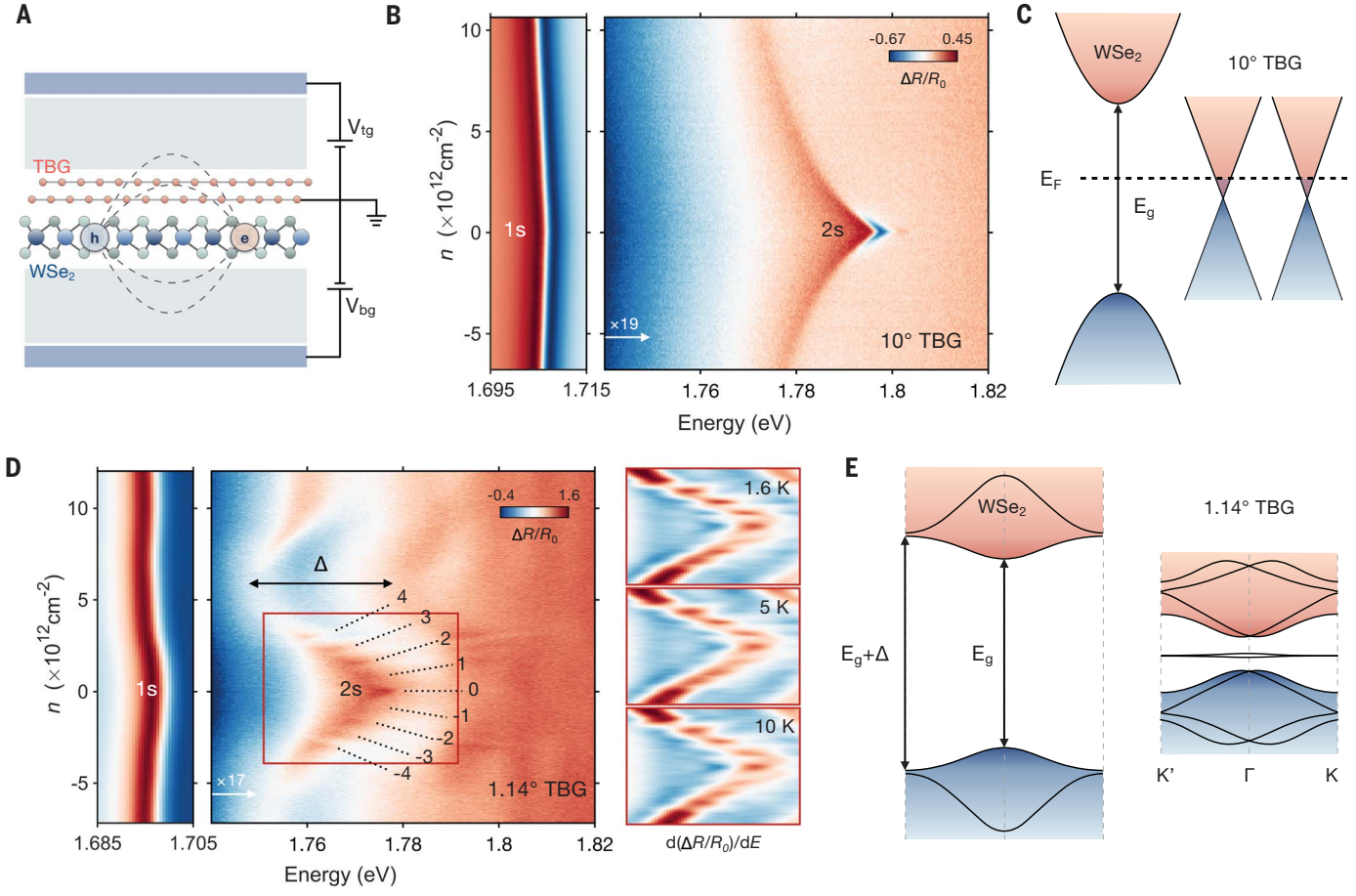

Fig. 2. Rydberg sensing of WSe_2 adjacent to 10° and 1.14° TBG. (**A**) Schematic structure of a typical device with electrically grounded TBG and monolayer WSe_2 embedded in hBN/graphite dual gates. (**B**) Doping-dependent reflectance contrast ($\Delta R/R_0$) spectrum of device D1 with 10° TBG (λ/r_B = 0.2). The WSe_2 serves as a dielectric sensor, whose 2s exciton energy reflects the dielectric screening of the neighboring TBG. (**C**) Schematic band alignment between monolayer WSe_2 and 10° TBG. (**D**) Doping-dependent $\Delta R/R_0$ spectrum of device D2 with 1.14° TBG (λ/r_B = 1.9). Sawtooth features appear at filling factors −4 to 4 (highlighted by the red rectangle), and a replica is observed at higher energies of Δ = 32 meV. The right three panels show the temperature-insensitive sawtooth features at 1.6, 5, and 10 K, respectively. (**E**) Schematic band structure of near-magic-angle TBG and the adjacent monolayer WSe_2. The TBG features gap openings and flat bands, which result in the band insulating states (ν = ±4) and the cascade of symmetry-breaking phase transitions (ν = 0, ±1, ±2, ±3) observed in (D), respectively. Meanwhile, the spatially periodic screening of TBG folds the band of WSe_2 into the mini-Brillouin zone, generating a new optically allowed transition at $E_g + \Delta$. The $\Delta R/R_0$ spectra above 1.74 eV in (B) and (D) are multiplied by a factor of 19 and 17, respectively, for better illustration.

hole of the exciton, while the trend to minimize the repulsion energy will push the electron of the exciton toward the AB/BA-stacked regions, as schematically shown in the inset of Fig. 3D. The role of electron and hole is reversed on the hole-doped side. This process renders a spatial separation of the electron–hole pair, supporting a charge-transfer–type exciton that typically only forms in molecular crystals with electron or hole occupying adjacent molecules or across an interface between two kinds of materials (*49*).

In this scenario, with one charge residing at the AA site and the other charge mostly on the AB/BA site, the electron and hole of the Rydberg exciton have highly asymmetric electrical potential energies. The E_{shift} can then be approximately estimated from the difference in attraction on the AA site and repulsion on the AB/BA site as $E_{shift} \approx (eU_{AA} - eU_{AB/BA}) \propto (n_{AA} - n_{AB/BA})$, where U_{AA} ($U_{AB/BA}$) and n_{AA} ($n_{AB/BA}$) are the electric potential and carrier density at the AA (AB/BA) site, respectively. Quantitatively, the calculated $n_{AA} - n_{AB/BA}$ as a function of n/n_s is presented in Fig. 3D, where a nonmonotonic trend similar to that of E_{shift} is observed, with the critical densities (n_m) almost identical to our experimental observations on both the electron and hole-doped sides. As the doping reaches n_m, where LDOS of TBG nearly equalizes at the two sites, the charge density at the AB/BA site begins to grow faster than that in the AA site (see detailed charge-filling maps in fig. S7), and the lattice becomes more evenly filled at higher doping densities. Such a process explains the blue shift for X_{RM} at $|n| > |n_m|$ and the convergence of the multiple branches in the large density limit.

Meanwhile, considering the size of the 2s exciton (r_B ~ 7 nm, which could be underestimated here owing to the enhanced screening effect) that is about an order of magnitude larger than the interlayer spacing d (≈0.5 nm), the interlayer Coulomb interaction with TBG charges can be much stronger than the intralayer one. It is thus possible to see the pronounced energy shift of the lowest-energy branch that is much larger than its original binding energy after the TBG is doped. We reproduced these results in another ~0.6° device and performed control experiments by inserting additional hBN spacers to increase the interlayer distance, as shown in fig. S9. The

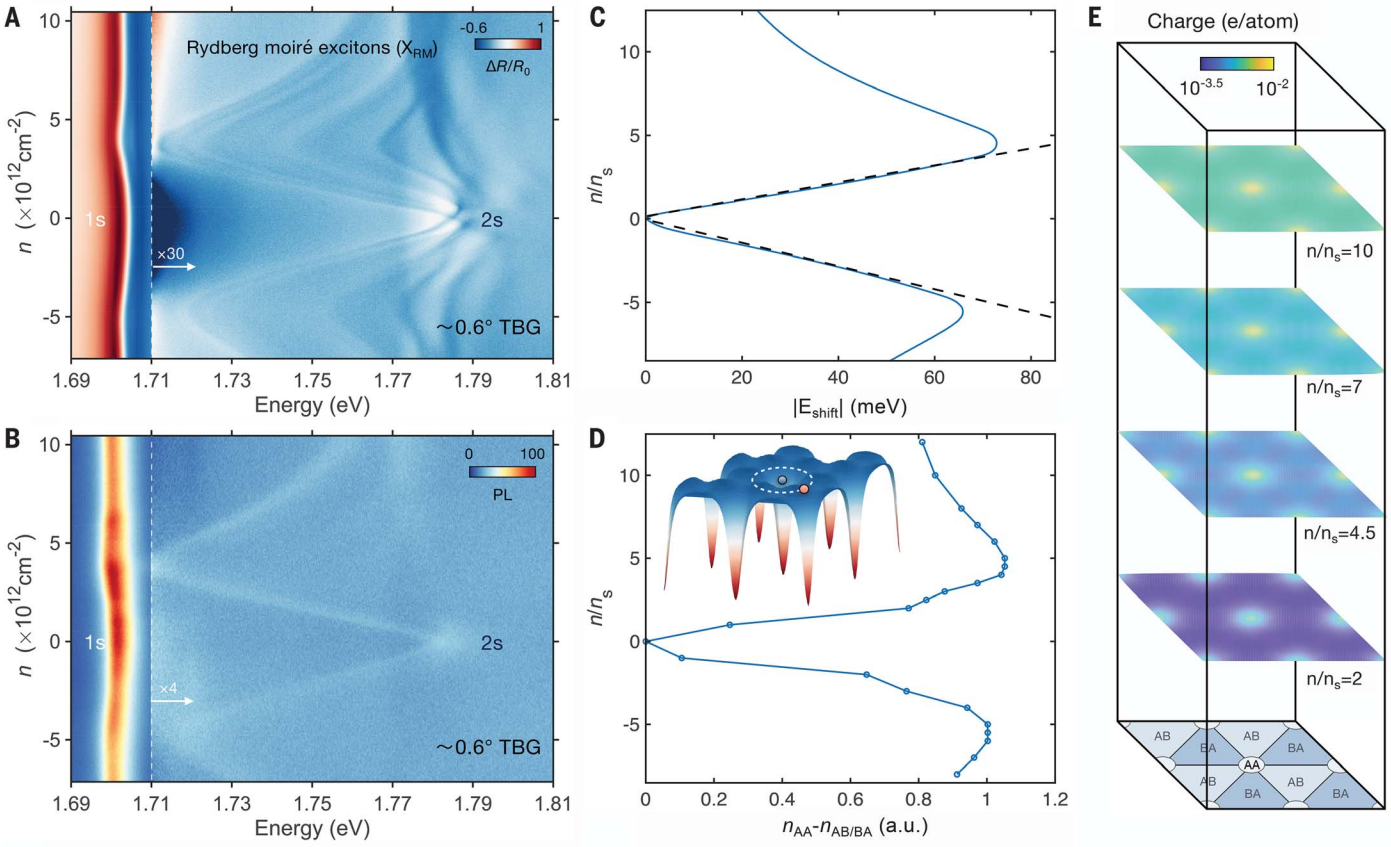

Fig. 3. Rydberg moiré exciton formation in WSe_2 adjacent to 0.6° TBG. (**A**) Reflectance contrast spectrum of device D3 with 0.6° TBG (λ/r_B = 3.6). The WSe_2 2s exciton resonance splits into multiple branches and exhibits nonmonotonic dependences when the TBG is doped. The $\Delta R/R_0$ spectra above 1.71 eV are multiplied by 30. (**B**) Photoluminescence spectrum of device D3 measured at the same location. (**C**) Extracted energy shift of the lowest-energy branch in (A) as a function of n/n_s (n_s denoting the full filling density of the first moiré band). (**D**) The calculated local carrier density difference between the AA and AB/BA sites with varying n/n_s. Insets are the schematic exemplification of the lowest-energy X_{RM} confinement on the electron-doped side. The moiré potential landscape facilitates the charge-transfer–type exciton configuration with the hole (blue sphere) residing on the AA site and the electron (red sphere) on the AB/BA site. The $n_{AA} - n_{AB/BA}$ versus n/n_s approximately reproduces the energy shift in (C) as $E_{shift} \approx (eU_{AA} - eU_{AB/BA}) \propto (n_{AA} - n_{AB/BA})$. a.u., arbitrary units. (**E**) Calculated spatial charge distribution (in logarithmic scales) of 0.6° TBG at representative doping densities. The lowest map is a schematic of relaxed TBG moiré superlattices with AA, AB, and BA sites marked.

energy shift is then strongly suppressed, and the system exhibits characteristics with weak interlayer interactions (*37*).

Crossover between the weak and strong coupling regimes

To better reveal the evolution to the strong coupling regime, more devices were fabricated and measured with twist angles ranging from ~0.6° to 1.23°, as presented in Fig. 4A. Reflection contrast and photoluminescence of additional devices are given in fig. S10. As the twist angle becomes smaller, the maximum red shift (denoted as E_m, at the critical density n_m) of the 2s state or the lowest-energy X_{RM} keeps growing, accompanied by the emergence of more replica states. Notably, as shown in the bottom-right panel of Fig. 4A, the energy separation between 1s and 2s states at n_m nearly vanishes in the smallest-twist-angle device where θ is slightly smaller than 0.6°, suggesting a strong interlayer Coulomb interaction of the X_{RM} that is even comparable to the binding energy of the 1s state and the possibility of forming new molecular states (*50*).

We summarize the twist-angle dependences of E_m and n_m on the electron-doped side in Fig. 4, B and C, respectively. The E_m is a direct evaluation of the maximum interlayer interaction, and the experimentally obtained n_m at three twist angles is in good agreement with that obtained from the theoretical calculations given in fig. S8. The n_m/n_s and E_m share a similar trend upon varying the angle θ, likely stemming from the positive correlation between charge accumulation at each moiré site and the interlayer Coulomb interaction energy. Meanwhile, an obvious reduction of X_{RM} linewidth (extracted for the lowest-energy branch) from ~8 meV to ~1.5 meV is observed with decreasing the twist angle into the strong coupling regime (Fig. 4D). The reduced linewidth is consistent with our interpretation of X_{RM} where the spatially separated electron–hole configuration is likely to support longer coherent lifetimes.

In this study, we developed and experimentally demonstrated a method for spatially confining and manipulating Rydberg excitons using long-wavelength moiré potentials. The strongly bound X_{RM} complex can be dominated by interlayer interactions and approach the energy of ground-state excitons. The system provides easy access to control the potential well depth by electrostatic doping, to tune the moiré wavelength by the twist angle, and to achieve longer lifetimes guaranteed by the electron–hole separation. All these features would be helpful for further realizing excitonic Rydberg-Rydberg interactions and coherent controls. Our study could open up unprecedented opportunities for the implementation of quantum information processing

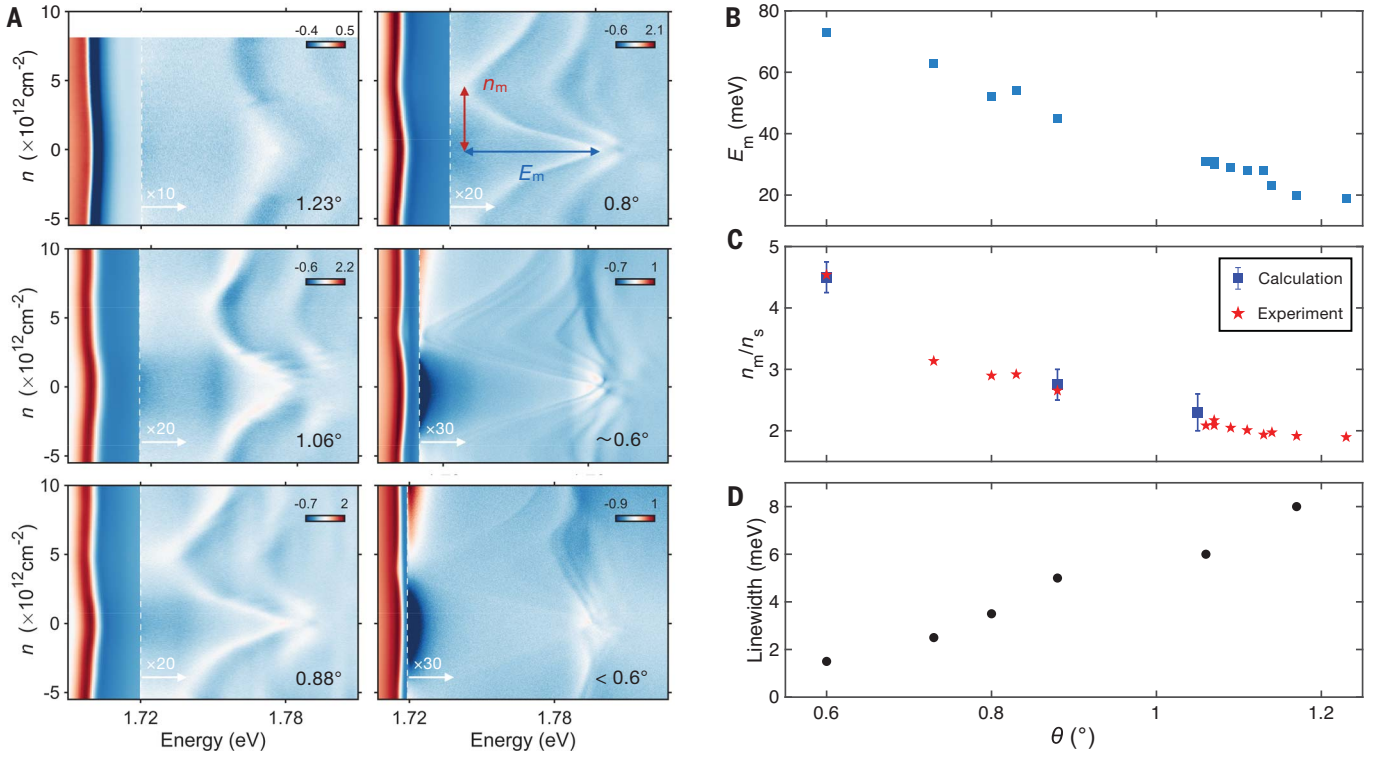

Fig. 4. Twist-angle dependences and crossover to the strong coupling regime. (**A**) Doping-dependent reflectance contrast spectra of devices with 1.23°, 1.06°, 0.88°, 0.8°, ~0.6°, and <0.6° TBG. The nearly parallel 2s resonance and replica evolve into X_{RM} with increasing λ/r_B (decreasing twist angle). (**B** to **D**) Twist-angle dependence of the maximum energy shift E_m (B), the normalized critical density n_m/n_s (C), and the estimated linewidth (D) extracted from the 2s resonance or the lowest-energy branch of X_{RM} on the electron-doped side. The critical density expected from the calculated $n_{AA} - n_{AB/BA}$ is marked in blue (C), in good agreement with the experimental results. The strongly reduced optical linewidth for θ < ~0.9° is an indication of longer coherent lifetimes of the X_{RM}, in accordance with its charge-transfer character in the strong coupling regime.

and quantum simulation based on the versatile Rydberg states in solid-state systems (*9*, *10*).

REFERENCES AND NOTES

1. T. F. Gallagher, *Rep. Prog. Phys.* **51**, 143–188 (1988).
2. N. Šibalić, C. S. Adams, *Rydberg Physics* (IOP Publishing, 2018).
3. M. Aßmann, M. Bayer, *Adv. Quantum Technol.* **3**, 1900134 (2020).
4. M. Saffman, T. G. Walker, K. Mølmer, *Rev. Mod. Phys.* **82**, 2313–2363 (2010).
5. E. Urban *et al.*, *Nat. Phys.* **5**, 110–114 (2009).
6. H. Weimer, M. Müller, I. Lesanovsky, P. Zoller, H. P. Büchler, *Nat. Phys.* **6**, 382–388 (2010).
7. H. Labuhn *et al.*, *Nature* **534**, 667–670 (2016).
8. D. Bluvstein *et al.*, *Science* **371**, 1355–1359 (2021).
9. A. N. Poddubny, M. M. Glazov, *Phys. Rev. Lett.* **123**, 126801 (2019).
10. J. Taylor *et al.*, *Quantum Sci. Technol.* **7**, 035016 (2022).
11. K. He *et al.*, *Phys. Rev. Lett.* **113**, 026803 (2014).
12. A. Chernikov *et al.*, *Phys. Rev. Lett.* **113**, 076802 (2014).
13. A. Raja *et al.*, *Nat. Commun.* **8**, 15251 (2017).
14. A. V. Stier *et al.*, *Phys. Rev. Lett.* **120**, 057405 (2018).
15. K. F. Mak, D. Xiao, J. Shan, *Nat. Photonics* **12**, 451–460 (2018).
16. G. Wang *et al.*, *Rev. Mod. Phys.* **90**, 021001 (2018).
17. Y. Xu *et al.*, *Nature* **587**, 214–218 (2020).
18. Z. Zhang *et al.*, *Nat. Phys.* **18**, 1214–1220 (2022).
19. A. Popert *et al.*, *Nano Lett.* **22**, 7363–7369 (2022).
20. Y. Xu *et al.*, *Nat. Mater.* **20**, 645–649 (2021).
21. K. L. Seyler *et al.*, *Nature* **567**, 66–70 (2019).
22. K. Tran *et al.*, *Nature* **567**, 71–75 (2019).
23. C. Jin *et al.*, *Nature* **567**, 76–80 (2019).
24. E. M. Alexeev *et al.*, *Nature* **567**, 81–86 (2019).
25. N. P. Wilson, W. Yao, J. Shan, X. Xu, *Nature* **599**, 383–392 (2021).
26. D. Huang, J. Choi, C. K. Shih, X. Li, *Nat. Nanotechnol.* **17**, 227–238 (2022).
27. E. C. Regan *et al.*, *Nat. Rev. Mater.* **7**, 778–795 (2022).
28. M. H. Naik *et al.*, *Nature* **609**, 52–57 (2022).
29. R. A. Suris, *Optical Properties of 2D Systems with Interacting Electrons* (Springer Netherlands, 2003).
30. A. V. Koudinov *et al.*, *Phys. Rev. Lett.* **112**, 147402 (2014).
31. Y. C. Chang, S. Y. Shiau, M. Combescot, *Phys. Rev. B* **98**, 235203 (2018).
32. M. Sidler *et al.*, *Nat. Phys.* **13**, 255–261 (2017).
33. D. K. Efimkin, A. H. MacDonald, *Phys. Rev. B* **95**, 035417 (2017).
34. C. Fey, P. Schmelcher, A. Imamoglu, R. Schmidt, *Phys. Rev. B* **101**, 195417 (2020).
35. K. Wagner *et al.*, *Phys. Rev. Lett.* **125**, 267401 (2020).
36. E. Liu *et al.*, *Nat. Commun.* **12**, 6131 (2021).
37. See supplementary materials.
38. A. C. Riis-Jensen, J. Lu, K. S. Thygesen, *Phys. Rev. B* **101**, 121110 (2020).
39. Y. Cao *et al.*, *Nature* **556**, 80–84 (2018).
40. X. Lu *et al.*, *Nature* **574**, 653–657 (2019).
41. D. Wong *et al.*, *Nature* **582**, 198–202 (2020).
42. U. Zondiner *et al.*, *Nature* **582**, 203–208 (2020).
43. R. Bistritzer, A. H. MacDonald, *Proc. Natl. Acad. Sci. U.S.A.* **108**, 12233–12237 (2011).
44. L. Balents, C. R. Dean, D. K. Efetov, A. F. Young, *Nat. Phys.* **16**, 725–733 (2020).
45. E. Y. Andrei, A. H. MacDonald, *Nat. Mater.* **19**, 1265–1275 (2020).
46. T. Smoleński *et al.*, *Nature* **595**, 53–57 (2021).
47. Y. Shimazaki *et al.*, *Phys. Rev. X* **11**, 021027 (2021).
48. H. Yoo *et al.*, *Nat. Mater.* **18**, 448–453 (2019).
49. X. Y. Zhu, Q. Yang, M. Muntwiler, *Acc. Chem. Res.* **42**, 1779–1787 (2009).
50. I. Schwartz *et al.*, *Science* **374**, 336–340 (2021).
51. Q. Hu *et al.*, Data repository for "Observation of Rydberg moiré excitons," version 1, Zenodo (2023); https://doi.org/10.5281/zenodo.7944742.

ACKNOWLEDGMENTS

We thank X. Cui for helpful discussions. **Funding:** This work was supported by the National Key R&D Program of China (grant nos. 2021YFA1401300, 2021YFA1400900, 2021YFA0718300, 2021YFA1402100, and 2022YFA1402704), the National Natural Science Foundation of China (grant nos. 12174439, 11974263, 12174291, 61835013, 12174461, 12234012, 12104491, U1932215, and 12274186), the Strategic Priority Research Program of the Chinese Academy of Sciences (grant no. XDB33010100), the Innovation Program for Quantum Science and Technology (grant no. 2021ZD0302400), Supercomputing Center of Wuhan University, and the Synergetic Extreme Condition User Facility (SECUF). Z.Z. was partially supported by the European Union's Horizon 2020 research and innovation programme under the Marie Skłodowska-Curie grant no. 101034131 and the "Severo Ochoa" Programme for Centres of Excellence in R&D (CEX2020-001039-S/AEI/10.13039/501100011033). The growth of hBN crystals was supported by the Elemental Strategy Initiative of MEXT, Japan,

and CREST (JPMJCR15F3), JST. **Author contributions:** Y.X. and S.Y. conceived of and supervised the project. Q.H., H.C., F.J., X.Z., M.Z., and Z.W. built the experimental setup under the supervision of Q.Z., X.C., and Y.X. Q.H. fabricated the devices, performed the measurements, and analyzed the data. K.W. and T.T. grew the bulk hBN crystals. Z.Z., Y.Z., and S.Y. performed the theoretical calculations, with substantial input from F.W. and W.-M.L. Q.H. and Y.X. designed the scientific objectives. Q.H., Z.Z., S.Y., and Y.X. co-wrote the manuscript. All authors discussed the results and commented on the manuscript. **Competing interests:** The authors declare no competing interests. **Data and materials availability:** All data are available in this paper or the supplementary materials or are deposited at Zendo (*51*).

SUPPLEMENTARY MATERIALS

science.org/doi/10.1126/science.adh1506
Materials and Methods
Supplementary Text
Figs. S1 to S10
References (*52*–*63*)

Submitted 15 February 2023; accepted 24 May 2023
10.1126/science.adh1506

Observation of Rydberg moiré excitons

Qianying Hu, Zhen Zhan, Huiying Cui, Yalei Zhang, Feng Jin, Xuan Zhao, Mingjie Zhang, Zhichuan Wang, Qingming Zhang, Kenji Watanabe, Takashi Taniguchi, Xuewei Cao, Wu-Ming Liu, Fengcheng Wu, Shengjun Yuan, and Yang Xu

Science, **380** (6652), .
DOI: 10.1126/science.adh1506

Editor's summary
Rydberg states are excited states of atoms and molecules, the "inflated size" of which provides enhanced interactions that can be used in quantum simulators and sensor applications. Hu *et al*. showed that optically excited Rydberg excitons (excited Coulomb-bound electron-hole pairs) in monolayer tungsten diselenide could be confined and controlled using the narrow and sharp potential wells of a moiré lattice generated in an adjacent small-angle twisted bilayer graphene. The generation, trapping, and eventual controlled interactions between Rydberg excitons held in a moiré lattice would be useful for developing a solid-state platform for quantum simulation and sensing. —Ian S. Osborne